Chemical Science

ROYAL SOCIETY OF CHEMISTRY

EDGE ARTICLE

View Article Online
View Journal | View Issue

Check for updates

Cite this: *Chem. Sci.*, 2022, **13**, 12673

All publication charges for this article have been paid for by the Royal Society of Chemistry

Open Access Article. Published on 18 2022. Downloaded on 14/09/25 08:51:03.
This article is licensed under a Creative Commons Attribution-NonCommercial 3.0 Unported Licence.

Tandem electrocatalytic CO_2 reduction with Fe-porphyrins and Cu nanocubes enhances ethylene production†

Min Wang,‡[a] Vasilis Nikolaou, ‡[b] Anna Loiudice,[ac] Ian D. Sharp, [c] Antoni Llobet *[bd] and Raffaella Buonsanti *[a]

Received 27th August 2022
Accepted 18th October 2022

DOI: 10.1039/d2sc04794b

rsc.li/chemical-science

Copper-based tandem schemes have emerged as promising strategies to promote the formation of multi-carbon products in the electrocatalytic CO_2 reduction reaction. In such approaches, the CO-generating component of the tandem catalyst increases the local concentration of CO and thereby enhances the intrinsic carbon–carbon (C–C) coupling on copper. However, the optimal characteristics of the CO-generating catalyst for maximizing the C_2 production are currently unknown. In this work, we developed tunable tandem catalysts comprising iron porphyrin (**Fe-Por**), as the CO-generating component, and Cu nanocubes (**Cucub**) to understand how the turnover frequency for CO (TOF_{CO}) of the molecular catalysts impacts the C–C coupling on the Cu surface. First, we tuned the TOF_{CO} of the **Fe-Por** by varying the number of orbitals involved in the π-system. Then, we coupled these molecular catalysts with the Cu_{cub} and assessed the current densities and faradaic efficiencies. We discovered that all of the designed **Fe-Por** boost ethylene production. The most efficient Cu_{cub}/**Fe-Por** tandem catalyst was the one including the **Fe-Por** with the highest TOF_{CO} and exhibited a nearly 22-fold increase in the ethylene selectivity and 100 mV positive shift of the onset potential with respect to the pristine Cu_{cub}. These results reveal that coupling the TOF_{CO} tunability of molecular catalysts with copper nanocatalysts opens up new possibilities towards the development of Cu-based catalysts with enhanced selectivity for multi-carbon product generation at low overpotential.

Introduction

The electrochemical CO_2 reduction reaction (CO_2RR) offers the opportunity to convert CO_2 into fuels and chemical feedstocks, while mitigating anthropogenic CO_2 emissions and storing renewable energy.[1,2] Multi-carbon (C_{2+}) compounds (*e.g.*, ethylene, ethanol, propanol) are among the most attractive CO_2RR products owing to their commercial value and high energy densities.[1,2] However, optimizing the activity of CO_2RR electrocatalysts towards one particular product remains a crucial challenge that is not trivial to address because multiple intermediates are involved in the CO_2 to C_{2+} conversion pathway.[3–5]

Cu-based materials have been widely employed as CO_2RR catalysts due to their unique ability to facilitate the electroreduction of CO_2 beyond two electron reduction products.[5,6] Numerous studies on catalyst development and mechanistic investigations have demonstrated that the surface coverage of the adsorbed CO (indicated as *CO) regulates the activation barrier of the C–C coupling step and, thus, the formation of C_{2+} products.[7–9] An attractive approach to realize this high *CO surface coverage is *via* tandem catalysis, wherein Cu is coupled with a CO-producing component to realize the sequential CO_2-to-CO and CO-to-C_{2+} product conversion on complementary active sites that are coupled at the nanometer scale.[10–21] However, the correlation between the intrinsic catalytic properties of the CO-generating component (*e.g.* turnover frequency, TOF, and overpotential) and its impact on the outcome of tandem catalysis (*e.g.* C–C coupling efficiency) is still critically missing. Thus, the fundamental design principles required to rationally promote C_{2+} production while decreasing the overpotential in tandem catalysis remain to be elucidated.

Bimetallic systems comprising Cu and another metal (Au, Ag, or Zn) as the CO-producing component have been extensively investigated as electrocatalysts in tandem CO_2

[a]*Laboratory of Nanochemistry for Energy (LNCE), Institute of Chemical Sciences and Engineering (ISIC), École Polytechnique Fédérale de Lausanne, CH-1950 Sion, Switzerland. E-mail: raffaella.buonsanti@epfl.ch*

[b]*Institute of Chemical Research of Catalonia (ICIQ), Barcelona Institute of Science and Technology (BIST), 43007, Tarragona, Spain. E-mail: allobet@iciq.cat*

[c]*Walter Schottky Institute and Physics Department, Technische Universität München, Am Coulombwall 4, 85748 Garching, Germany*

[d]*Departament de Química, Universitat Autònoma de Barcelona (UAB), Cerdanyola del Vallès, 08193 Barcelona, Spain*

† Electronic supplementary information (ESI) available. See DOI: https://doi.org/10.1039/d2sc04794b

‡ These authors have equally contributed.

© 2022 The Author(s). Published by the Royal Society of Chemistry

Open Access Article. Published on 18 2022. Downloaded on 14/09/25 08:51:03.
This article is licensed under a Creative Commons Attribution-NonCommercial 3.0 Unported Licence.

reduction.[15–21] One drawback of these catalysts is that composition (*e.g.* alloying) and morphology can change during operation.[15–18] These changes affect both the physical and electronic structure, thus complicating the interpretation of the catalytic behavior and delaying the establishment of design principles required to further improve the catalytic activity of these systems.[18–22] Additionally, tuning the intrinsic activity and efficiency of metals is difficult and requires their coupling with organic modifiers.[23,24] Consequently, these systems are not ideal for guiding the understanding of the performance-determining factors in tandem catalysis.

Recent studies have suggested that CO-producing molecular catalysts are alternative candidates to metals in tandem schemes.[25–27] Molecular components offer additional versatility compared to metals because their electronic and structural features can be tuned *via* synthetic modifications.[28–31] While the examples are still limited, studies in the literature on tandem catalysts including CO-producing molecular catalysts and Cu are encouraging.[25–27] For example, the addition of either an iron porphyrin or a cobalt phthalocyanine to sputtered Cu resulted in enhanced C_{2+} product yields.[25,26] Specifically, the coupling of iron porphyrin with sputtered Cu resulted in increased faradaic efficiency for ethanol from 29% to 41% and in a shift the detection potential of this product from −0.84 to −0.82 V *vs.* RHE.[25] The cobalt phthalocyanine/Cu catalyst enhanced the faradaic efficiency for C_{2+} products from 45% to 82% in a highly basic electrolyte.[26] Instead, the combination of a cobalt phthalocyanine with a Zn–N–C catalyst promoted formation of methane with a total faradaic efficiency of 18%, a product not observed on the pristine Zn–N–C, again in a highly basic electrolyte.[27] However, these studies have so far focused only on the integration of commercial molecular catalysts in tandem CO_2RR, thus not profiting from the chemical tunability of these systems. Furthermore, they remain a few isolated examples each utilizing a different electrocatalyst and with testing performed under different conditions, which make any comparison among them difficult to make.

Herein, we exploit the intrinsic tunability of molecular catalysts (in terms of TOF_{CO} and overpotential) to understand the impact of the CO-generating component on subsequent C–C coupling on Cu surfaces during tandem catalysis. Iron porphyrin (**F-Por**) molecular catalysts are selected as the CO-producing entity because of their high efficiency for CO_2 to CO conversion at neutral pH when immobilized on conductive substrates.[32–34] Furthermore, their versatile chemistry enables facile tuning of their redox behaviors *via* modification of the π-system.[35–37] To this end, we synthesized three **Fe-Por** with different numbers of orbitals involved in the π-system. Colloidally dispersible Cu nanocubes ($\mathbf{Cu_{cub}}$) were chosen as Cu catalysts. Their intrinsic selectivity towards C–C coupling, and ethylene production in particular, as well as the demonstrated possibility to integrate them in different electrochemical cell designs, justifies this choice.[38–41] Furthermore, the fact that both **Fe-Por** and $\mathbf{Cu_{cub}}$ catalysts can be employed as inks is beneficial for catalyst processability, scalability, and device integration. By studying the designed series of **Fe-Por** molecules in tandem CO_2RR, we investigate how their TOF_{CO} impacts the C–C coupling on $\mathbf{Cu_{cub}}$. Importantly, we discover that the most active **Fe-Por** generates an optimal local environment that boosts the intrinsic activity of $\mathbf{Cu_{cub}}$ towards ethylene while also increasing energy efficiency by anodically shifting the potential at which this product is detected.

Results and discussion

A series of **Fe-Por** complexes with a varying number of orbitals involved in the π-system of the porphyrin ligand were synthesized and tested as molecular catalysts for CO_2RR (Fig. 1). These complexes are iron(III)-chlorido-tetrabicyclo[2.2.2]octadiene-tetraphenyl porphyrin (**Fe-TbcTPP**), iron(III)-chlorido-tetraphenyl porphyrin (**Fe-TPP**), and an iron(III)-chlorido-tetrabenzo-tetraphenyl porphyrin (**Fe-TBTPP**). The synthesis of **Fe-TPP** was carried out following a procedure reported in the literature,[42] whereas **Fe-TbcTPP** and **Fe-TBTPP** were prepared according to the synthetic approach described in detail in the ESI and illustrated in Scheme S1†. In brief, the initial step corresponds to the synthesis of the free base porphyrin $\mathbf{H_2}$-**TbcTPP** *via* a "Lindsey condensation reaction".[43] Refluxing $\mathbf{H_2}$-**TbcTPP** in a tetrahydrofuran (THF) solution containing $FeBr_2$ and 2,6-lutidine generates the desired **Fe-TbcTPP**. The last step is a retro-Diels–Alder reaction achieved by heating the **Fe-TbcTPP** complex at 200 °C under vacuum to produce **Fe-TBTPP**. The ^{1}H and ^{13}C-NMR spectra of $\mathbf{H_2}$**TbcTPP** are presented in Fig. S1 and S2,† while the MALDI-TOF spectra of the iron-derivatives (**Fe-TbcTPP** and **Fe-TBTPP**) are provided in Fig. S3

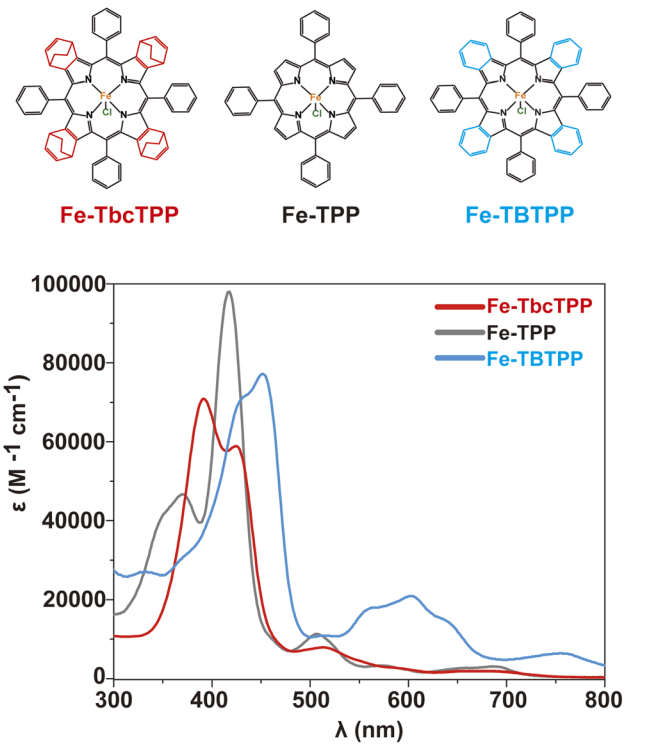

Fig. 1 The Fe-Por molecules synthesized and investigated as molecular catalysts in this study (top) along with the UV-vis spectra of the same in THF (bottom).

© 2022 The Author(s). Published by the Royal Society of Chemistry

Open Access Article. Published on 18 2022. Downloaded on 14/09/25 08:51:03.
This article is licensed under a Creative Commons Attribution-NonCommercial 3.0 Unported Licence.

and S4.† The aromatic delocalization effect in **Fe-Por** is revealed by optical absorption spectroscopy (Fig. 1 and Table S1†). According to expectation, as the number of π-orbitals contributing to the system increases, the respective Soret band red-shifts, following the peak wavelength (λ_{max}) order λ_{max} (**Fe-TBTPP**) > λ_{max} (**Fe-TPP**) > λ_{max} (**Fe-TbcTPP**).

To understand the impact of the different porphyrin ligands on the electrocatalytic properties, we performed cyclic voltammetry (CV) experiments in homogeneous conditions (Fig. 2 and ESI† for details). A very similar behavior was observed for all **Fe-Por**, with each characterized by three redox processes that are assigned to Fe^{III}/Fe^{II}, Fe^{II}/Fe^{I}, and Fe^{I}/Fe^{0}, as depicted in Fig. 2 and Table S1.† The second and third reduction waves are associated with two consecutive one electron reductions that are mainly ligand-based.[44,45] As expected, the different degree of π-delocalization of the **Fe-Por** results in a significant shift of the respective redox potentials. More specifically, the **Fe-TbcTPP** containing the more σ-donating and less π-accepting bicyclo [2.2.2]octadiene groups has the lowest potentials. On the other hand, the **Fe-TBTPP** containing benzo groups and phenyl substitution at the meso positions has more anodic values. The **Fe-TPP** with no additional functionalization onto the pyrrole moieties has redox potentials between those of **Fe-TbcTPP** and **Fe-TBTPP**.

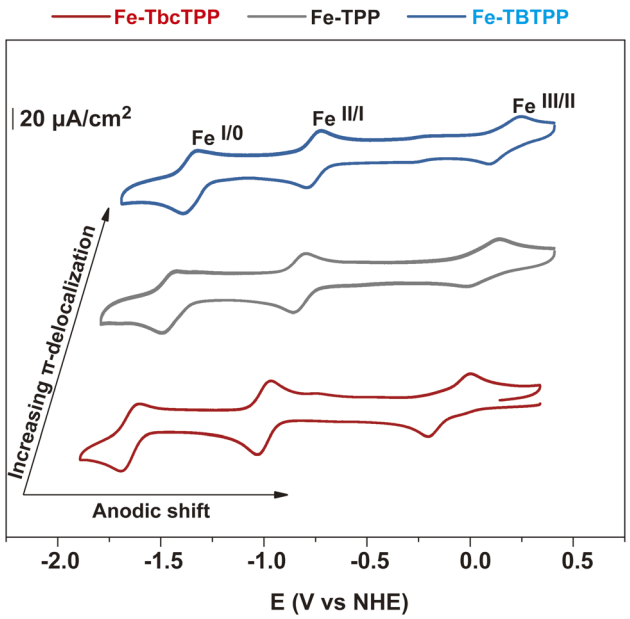

Fig. 2 Cyclic voltammetry of 0.25 mM **Fe-Por** dissolved in DMF containing 0.1 M $TBAPF_6$ as the supporting electrolyte, carried out at a scan rate of 100 mV s^{-1}. **Fe-TbcTPP** (red), **Fe-TPP** (gray), and **Fe-TBTPP** (blue).

We then investigated the CO_2RR catalytic properties of the **Fe-Por** in an H-cell using CO_2 saturated 0.1 M $KHCO_3$ as the electrolyte (see ESI† for details). Results of these experiments are presented in Fig. 3. Linear sweep voltammetry (LSV) (Fig. 3a) reveals an anodic shift of the onset potential (*i.e.* the potential at which the current starts to be detectable from the background) for CO_2 reduction from −0.57 V (**Fe-TbcTPP**) to −0.50 V (**Fe-TPP**) and to −0.40 V (**Fe-TBTPP**) *vs.* RHE (Reversible Hydrogen Electrode). This anodic shift follows the π-delocalization trend of the **Fe-Por** reported above.[46–48] Furthermore, the faradaic efficiency for CO (FE_{CO}) is higher for **Fe-TBTPP** than for either **Fe-TPP** or **Fe-TbcTPP** across the entire potential range (Fig. 3b and S5†), with a maximum of 91% at −0.55 V *vs.* RHE. The TOF_{CO} (see ESI† for details) follows the same trend, with TOF_{CO} (**Fe-TBTPP**) > TOF_{CO} (**Fe-TPP**) > TOF_{CO} (**Fe-TbcTPP**) (Fig. 3c). Specifically, **Fe-TBTPP** exhibits the highest TOF_{CO} (0.26 s^{-1}) compared to **Fe-TPP** (0.11 s^{-1}) and **Fe-TbcTPP** (0.02 s^{-1}) at −0.95 V *vs.* RHE.

Following the analysis of the **Fe-Por**, we prepared the $\mathbf{Cu_{cub}}$/**Fe-Por** by mixing the **Fe-Por** and the $\mathbf{Cu_{cub}}$ (Fig. S6†) (see ESI† for details). The inks were then drop cast onto glassy carbon electrodes and the activities of the tandem catalysts were tested from −0.45 V to −1.05 V *vs.* RHE. Fig. 4 and S7† provide an overview of the obtained data. At low potentials (−0.45 V and

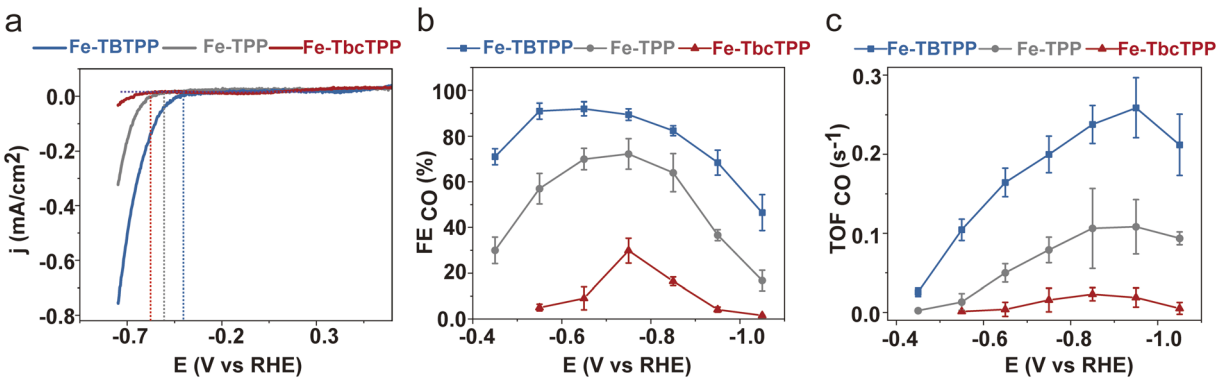

Fig. 3 (a) LSV curves of the **Fe-Por** catalysts measured at a scan rate of 10 mV s^{-1}, with the vertical dashed lines representing the onset potentials for each catalyst; (b) FE_{CO} and (c) TOF_{CO} as a function of applied potential. These measurements were performed at **Fe-Por** loadings of 16 nmol cm^{-2} on carbon nanotubes deposited onto glassy carbon electrodes ($S = 1.33$ cm^2) using an H-cell with CO_2 saturated 0.1 M $KHCO_3$ electrolyte. The carbon nanotubes were chosen as commonly used as a conductive support to homogeneously disperse the molecular catalysts *via* non-covalent interactions.[32–34] The reported FE and TOF values are the average of three independent experiments with error bars indicating the standard deviations.

© 2022 The Author(s). Published by the Royal Society of Chemistry

Open Access Article. Published on 18 2022. Downloaded on 14/09/25 08:51:03.
This article is licensed under a Creative Commons Attribution-NonCommercial 3.0 Unported Licence.

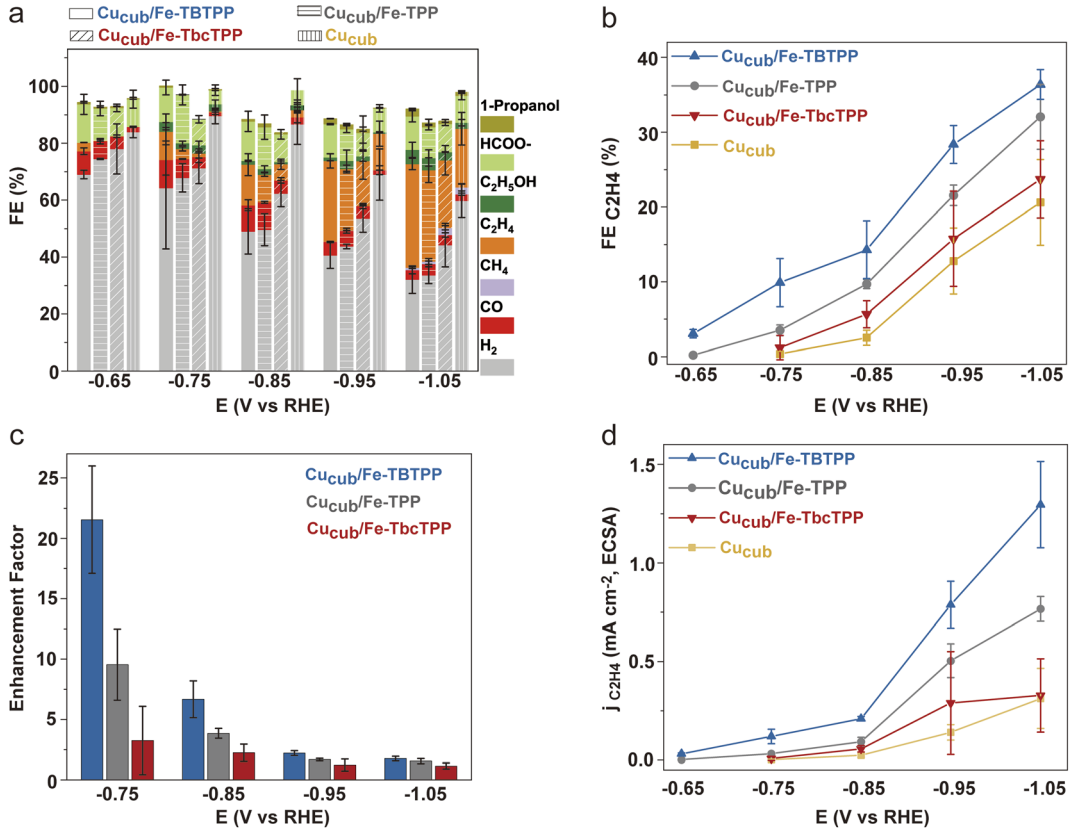

Fig. 4 (a) Total FEs and (b) $FE_{C_2H_4}$ for **Cu_{cub}/Fe-TBTPP**, **Cu_{cub}/Fe-TPP**, **Cu_{cub}/Fe-TbcTPP** and **Cu_{cub}** as a function of potential; (c) C_2H_4 product enhancement factor of the **Cu_{cub}/Fe-Por** compared to the pristine **Cu_{cub}** (enhancement factor = ($FE_{C_2H_4}$ of **Cu_{cub}/Fe-Por**)/($FE_{C_2H_4}$ of **Cu_{cub}**) as a function of potential; (d) $j_{C_2H_4/ECSA}$ for **Cu_{cub}/Fe-TBTPP**, **Cu_{cub}/Fe-TPP**, **Cu_{cub}/Fe-TbcTPP** and **Cu_{cub}** as a function of potential. The electrodes for these experiments were prepared by loading 3.12×10^2 nmol cm^{-2} of **Cu_{cub}** and 8 nmol cm^{-2} of the **Fe-Por** onto glassy carbon electrodes. The reported values are an average of three independent experiments with error bars indicating the standard deviations.

−0.55 V *vs.* RHE), the addition of the **Fe-Por** to **Cu_{cub}** suppresses the hydrogen evolution reaction (HER) and enhances the production of CO and formate. However, no evidence of C–C coupling reactions is observed at these potentials (Fig. S7†). The HER suppression and CO_2RR promotion induced by the **Fe-Por** become more pronounced at more negative potentials (−0.65 V to −1.05 V *vs.* RHE, Fig. 4a). Indeed, the enhancement of C_2H_4 faradaic efficiency from **Cu_{cub}/Fe-Por** relative to **Cu_{cub}** is clearly observed for all tandem-catalysts (Fig. 4b). Interestingly, C_2H_4 is produced at a potential as low as −0.65 V *vs.* RHE for the **Cu_{cub}/Fe-TBTPP**, which maintains the highest $FE_{C_2H_4}$ across the entire potential range (Fig. 4b), reaching a $FE_{C_2H_4}$ of 36% at −1.05 V *vs.* RHE. By comparison, the **Cu_{cub}** in the absence of **Fe-Por** only achieved a $FE_{C_2H_4}$ of 19% at the same potential. At more negative potential, CH_4 is favored over C_2H_4 (Fig. S8†). Thus, while Fe-TBTPP still promotes C–C coupling, the $FE_{C_2H_4}$ decreases (~25% at −1.15 V). The $FE_{C_2H_4}$ was much lower also for Cu_{sphere}/Fe-TBTPP (~15% at −1.05 V), which highlights the importance of the Cu morphology to maximize ethylene production (Fig. S9†).

To quantify the impact of the **Fe-Por** on C–C coupling, we define an enhancement factor for C_2H_4 production as the ratio of $FE_{C_2H_4}$ of **Cu_{cub}/Fe-Por** to the $FE_{C_2H_4}$ of **Cu_{cub}** at a given potential. The corresponding enhancement factors for **Cu/Fe-TBTPP**, **Cu/Fe-TPP** and **Cu/Fe-TbcPP** are 21.5, 9.5 and 3.2 at −0.75 V *vs.* RHE, respectively (Fig. 4c). Analysis of the electrochemically active surface area (ECSA) of **Cu_{cub}/Fe-Por** reveals a decreased solid/liquid contact area compared to the **Cu_{cub}**, which is likely a consequence of the blocking of Cu active sites by the molecules (Fig. S10†). However, the ECSA-normalized current density ($j_{C_2H_4/ECSA}$) indicates an increase in the intrinsic activity of the unpassivated sites in the presence of the **Fe-Por**, with a trend that is consistent with the FE and the enhancement factor (Fig. 4d).

To exclude the contribution of C_1 product suppression on the observed trends and to provide further evidence for the tandem mechanism, we analyzed the C_1 products in greater detail (Fig. 5). The FE_{C_1} and the $j_{C_1,ECSA}$ of the **Cu_{cub}/Fe-Por** catalysts are generally higher than those for the pristine **Cu_{cub}** across the entire potential range (Fig. 5a, b and S11†). Furthermore, the trend of FE_{C_1} and $j_{C_1/ECSA}$ among the **Cu_{cub}/Fe-Por** follows that of the $FE_{C_2H_4}$, which are higher values measured for higher molecular TOF_{CO}. The improved capacity of **Cu_{cub}** to catalyze C–C coupling at more negative potentials results in an increase of $FE_{C_{2+}}/FE_{C_1}$ for all catalysts at higher overpotentials (Fig. 5c). The decrease of FE_{CO} (Fig. 5d) and the saturation of j_{CO}

© 2022 The Author(s). Published by the Royal Society of Chemistry

Open Access Article. Published on 18 2022. Downloaded on 14/09/25 08:51:03.
This article is licensed under a Creative Commons Attribution-NonCommercial 3.0 Unported Licence.

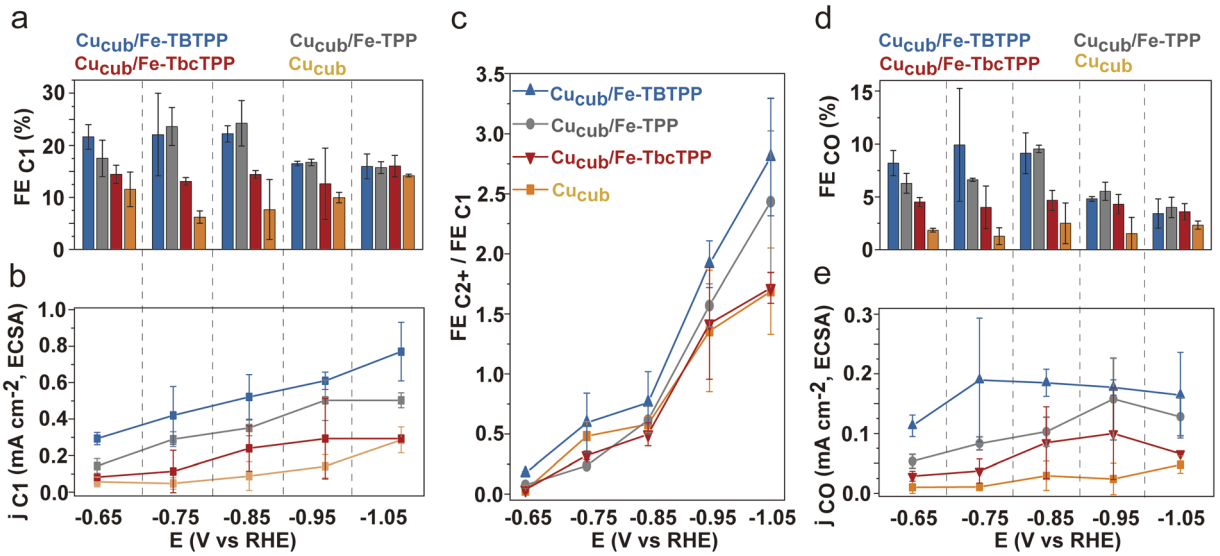

Fig. 5 (a) FE_{C_1} and (b) partial current density for the C_1 products (j_{C_1}) normalized by ECSA, (c) FE ratio of C_{2+} to C_1 products, (d) FEs and (e) partial current density for CO (j_{CO}) normalized by ECSA of **Cu_{cub}/Fe-TBTPP**, **Cu_{cub}/Fe-TPP**, **Cu_{cub}/Fe-TbcTPP** and **Cu_{cub}** at different potentials. The reported values are an average of three independent experiments with error bars indicating the standard deviations.

(Fig. 5e) with increasing overpotential is consistent with the increased consumption of CO as more ethylene is generated *via* the tandem catalytic mechanism. In contrast, FE_{CO} and j_{CO} remain approximately constant for pure **Cu_{cub}** across all potentials, reflecting the unmodified native activity of the nanocubes in the absence of tandem CO generation.

To investigate possible changes of electronic and chemical properties of **Cu_{cub}** due to interactions with the molecular constituents, which could influence the overall catalytic properties of the **Cu_{cub}/Fe-Por**, we performed X-ray photoelectron spectroscopy (XPS) (Fig. S12†). The analysis of the Cu 2p peaks and Cu LMM spectra indicated that Cu is present in its metallic form in all systems. Furthermore, the absence of any peak shifts in spectra from **Cu_{cub}/Fe-Por** compared to **Cu_{cub}** indicated that there are no changes in surface composition and/or charge transfer effects. This lack of a specific chemical or electronic change of the Cu surface, together with the systematic correlations between C–C coupling efficiency of **Cu_{cub}/Fe-Por** with the TOF_{CO} trends among **Fe-Por**, indicates that overall selectivity and activity is governed by the tandem catalytic process.

Having established that a tandem mechanism is dominant in defining activity and selectivity of **Cu_{cub}/Fe-Por**, optimization of ethylene production requires understanding of the relationship between the loading of the CO-generating component and the CO conversion rate of the Cu catalyst. With this aim, we tested the impact of **Fe-Por** loading on enhancing C–C coupling in **Cu_{cub}/Fe-Por** tandem catalysts (Fig. 6). We observe that the $FE_{C_2H_4}$ increases with the **Fe-Por** loading until reaching its maximum value at 8 nmol cm^{-2} (Fig. 6a). This trend suggests that addition of more **Fe-Por** results in the local accumulation of CO in the vicinity of **Cu_{cub}**, which promotes C–C coupling. However, a further increase of the **Fe-Por** coverage leads to decreased C_2H_4 selectivity. Concomitantly, the FE_{CO} increases

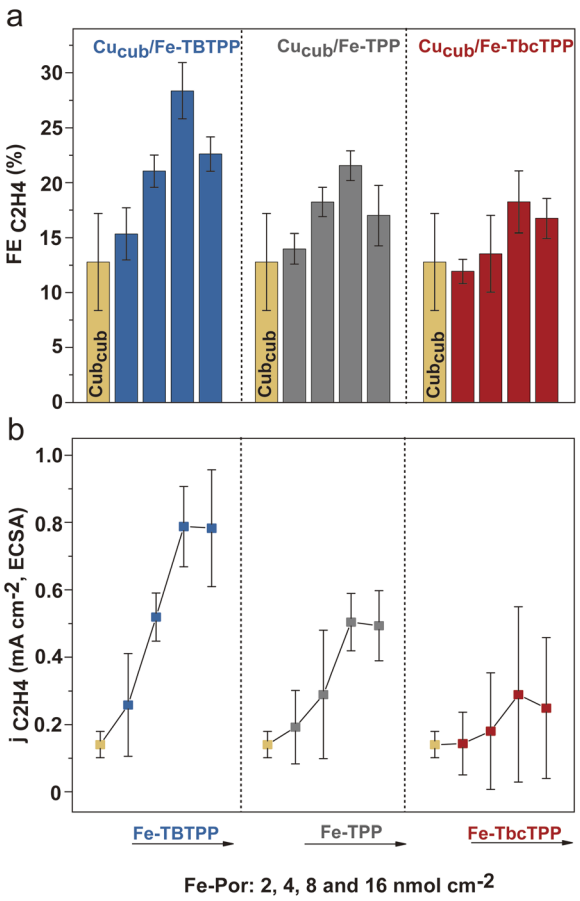

Fig. 6 (a) $FE_{C_2H_4}$ and (b) $j_{C_2H_4/ECSA}$ of **Cu_{cub}/Fe-TBTPP**, **Cu_{cub}/Fe-TPP**, **Cu_{cub}/Fe-TbcTPP** and **Cu_{cub}** at different loadings of the **Fe-Por** (2, 4, 8 and 16 nmol cm^{-2}) at −0.95 V *vs.* RHE in CO_2 saturated 0.1 M $KHCO_3$ H-cell. The reported values are an average of three independent experiments with error bars indicating the standard deviations.

© 2022 The Author(s). Published by the Royal Society of Chemistry

Open Access Article. Published on 18 2022. Downloaded on 14/09/25 08:51:03.
This article is licensed under a Creative Commons Attribution-NonCommercial 3.0 Unported Licence.

(Fig. S13†), which indicates that the additionally generated CO escapes the system.

As discussed above, the **Fe-Por** molecules also block Cu active sites. Consistent with this conclusion, we observe a continuous decrease of the ECSA with increased loading (Fig. S14†). The enhancement in intrinsic activity of the unpassivated sites on the $\mathbf{Cu_{cub}}$ compensates the decreasing concentration of sites, but only up to a certain loading. Above that point, the C_2H_4 selectivity is suppressed, which is also reflected in the $j_{C_2H_4,ECSA}$ (Fig. 6b). In particular, the $j_{C_2H_4,ECSA}$ in $\mathbf{Cu_{cub}}$/**Fe-Por** increases up to 8 nmol cm^{-2} and thereafter saturates.

The comparison of different **Fe-Por** at the same loadings reveals more efficient C_2H_4 production for the $\mathbf{Cu_{cub}}$/**Fe-TBTPP**. Furthermore, we note that lower loadings of the **Fe-TBTPP** generate higher $FE_{C_2H_4}$ and $j_{C_2H_4/ECSA}$ compared to higher loadings of the **Fe-TbcTPP** (*e.g.* 4 nmol cm^{-2} of **Fe-TBTPP** *vs.* 8 nmol cm^{-2} of **Fe-TbcTPP**). As the **Fe-TBTPP** possesses the highest TOF_{CO}, these data prove that the CO production rate plays a crucial role in achieving optimal C–C coupling in the tandem catalysts.

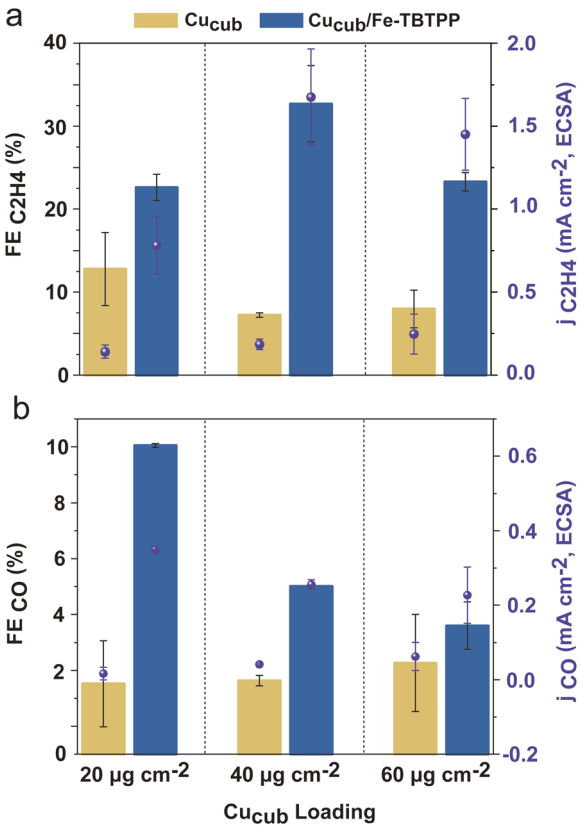

Fig. 7 (a) FE and partial current density for the C_2H_4 product normalized by ECSA ($j_{C_2H_4,ECSA}$) and (b) FE and partial current density for the CO product normalized by ECSA ($j_{CO,ECSA}$) for $\mathbf{Cu_{cub}}$/Fe-TBTPP at different loading of $\mathbf{Cu_{cub}}$ (3.12×10^2, 6.24×10^2 and 9.36×10^2 nmol cm^{-2}) with the same Fe-TBTPP loading (16 nmol cm^{-2}) at −0.95 V *vs.* RHE in the CO_2 saturated 0.1 M $KHCO_3$ H-cell. The reported values are an average of three independent experiments with error bars indicating the standard deviations.

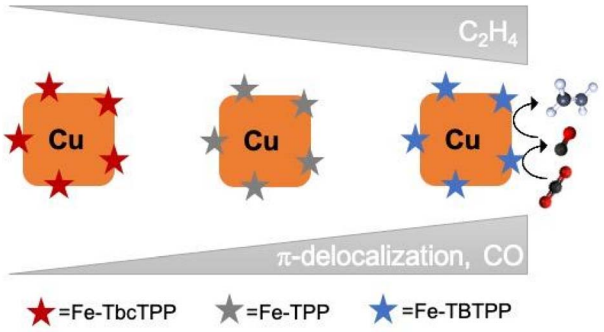

Fig. 8 Schematic representation of the proposed mechanism for C_2H_4 promotion in $\mathbf{Cu_{cub}}$/Fe-Por tandem catalysts. The C–C coupling enhancement and C_2H_4 promotion correlate with the Fe-Por selectivity and conversion rate for CO.

To test whether the bottleneck for further improving C_2H_4 generation with the highest **Fe–Por** loading is the CO consumption, we tested increased Cu-cube loadings for the best performing $\mathbf{Cu_{cub}}$/**Fe-TBTPP** (Fig. 7 and S15†). The **Fe-TBTPP** loading was kept at 16 nmol cm^{-2} for comparison with Fig. 6. An increase in $\mathbf{Cu_{cub}}$ loading from 3.12×10^2 to 6.24×10^2 nmol cm^{-2} does improve the C_2H_4 production, with both the $FE_{C_2H_4}$ and $j_{C_2H_4,ECSA}$ increasing (Fig. 7a). A $FE_{C_2H_4}$ of 33% is thus measured at −0.95 V *vs.* RHE. The concomitant decrease FE_{CO} and $j_{CO,ECSA}$ (Fig. 7b) indicates that the CO produced by **Fe-TBTPP** is indeed further consumed by the increased $\mathbf{Cu_{cub}}$ loading.

For higher $\mathbf{Cu_{cub}}$ loading (9.36×10^2 nmol cm^{-2}), the $FE_{C_2H_4}$ and $j_{C_2H_4,ECSA}$ decrease and the FE_{CO} and $j_{CO,ECSA}$ don't change further. In a similar manner to the **Fe-Por** loading experiments, the ratio between the CO-generating component and the CO conversion rate of the Cu catalyst must be balanced for optimal performance.

Finally, we characterized the **Fe-Por** by Fourier-transform infrared spectroscopy (FT-IR) and ultraviolet-visible spectroscopy (UV-vis) (Fig. S16 and S17†), and the $\mathbf{Cu_{cub}}$ morphology by TEM (Fig. S18†), which proved the intact structure of **Fe-Por** and cubic shape of $\mathbf{Cu_{cub}}$ after 1.5 hours of electrolysis. Furthermore, the best performing tandem catalyst in terms of C_2H_4 production, which is $\mathbf{Cu_{cub}}$/**Fe-TBTPP**, displayed an excellent stability and selectivity over 10 hours of electrolysis (Fig. S19†). Altogether, these data indicate that the addition of the **Fe-Por** has a stabilizing effect on the morphology of the Cu cubes. While a dedicated study is needed, we speculatively attribute the origin of this observation to the formation of the CO intermediate on a different surface than Cu.

Conclusions

In summary, we built tandem catalysts including **Fe-Por** with tunable CO_2 to CO selectivity (**Fe-TBTPP** > **Fe-TPP** > **Fe-TbcTPP**) and $\mathbf{Cu_{cub}}$. We discovered that the C–C coupling enhancement in these tandem catalysts correlates directly with the **Fe-Por** selectivity and conversion rates for CO, with the $\mathbf{Cu_{cub}}$/**Fe-TBTPP** being the best performing one.

© 2022 The Author(s). Published by the Royal Society of Chemistry

Open Access Article. Published on 18 2022. Downloaded on 14/09/25 08:51:03.
This article is licensed under a Creative Commons Attribution-NonCommercial 3.0 Unported Licence.

We found a 100 mV anodic potential shift for C_2H_4 detection, a 22 times enhancement of C_2H_4 production at −0.75 V *vs.* RHE and a doubled $FE_{C_2H_4}$ of 36% at −1.05 V *vs.* RHE in the **Cu_{cub}/Fe-TBTPP** compared to the **Cu_{cub}**. This performance is comparable to the state-of-the-art in this class of catalysts.[25–27] Going beyond it, these results demonstrate that the rate and potential at which CO is generated plays a defining role for the selectivity and overpotential of multiple-carbon products in tandem schemes (Fig. 8).

Overall, this study encourages further investigations on the design of the homogenous catalyst as a promising strategy to further optimize molecular-based tandem systems.

Data availability

Data for this paper, including UV-vis and electrochemical characterization, are available at Zenodo at **https://doi.org/10.5281/zenodo.7229402**.

Author contributions

M. W. carried out the synthesis of the tandem catalysts and all electrocatalytic testing for CO_2RR. V. N. synthesized and characterized the molecular catalysts. A. L. performed X-ray photoelectron spectroscopy and contributed to daily discussions. A. L. supervised the work on the molecular catalysts. I. S. contributed to discussions. R. B. supervised the work on the tandem catalysts and CO_2RR and coordinated the project. All the authors contributed to the writing of the manuscript.

Conflicts of interest

There are no conflicts to declare.

Acknowledgements

The authors gratefully acknowledge the support from EU-funded LICROX FET project (Grant agreement 951843).

References

1 X. Lim, *Nature*, 2015, **526**, 628–630.
2 H.-R. M. Jhong, S. Ma and P. J. A. Kenis, *Curr. Opin. Chem. Eng.*, 2013, **2**, 191–199.
3 Y. Y. Birdja, E. Pérez-Gallent, M. C. Figueiredo, A. J. Göttle, F. Calle-Vallejo and M. T. M. Koper, *Nat. Energy*, 2019, **4**, 732–745.
4 T. K. Todorova, M. W. Schreiber and M. Fontecave, *ACS Catal.*, 2020, **10**, 1754–1768.
5 S. Nitopi, E. Bertheussen, S. B. Scott, X. Liu, A. K. Engstfeld, S. Horch, B. Seger, I. E. L. Stephens, K. Chan, C. Hahn, J. K. Nørskov, T. F. Jaramillo and I. Chorkendorff, *Chem. Rev.*, 2019, **119**, 7610–7672.
6 A. A. Peterson, F. Abild-Pedersen, F. Studt, J. Rossmeisl and J. K. Nørskov, *Energy Environ. Sci.*, 2010, **3**, 1311–1315.
7 J. Li, Z. Wang, C. McCallum, Y. Xu, F. Li, Y. Wang, C. M. Gabardo, C. T. Dinh, T. T. Zhuang, L. Wang, J. Y. Howe, Y. Ren, E. H. Sargent and D. Sinton, *Nat. Catal.*, 2019, **2**(12), 1124–1131.
8 A. J. Garza, A. T. Bell and M. Head-Gordon, *ACS Catal.*, 2018, **8**(2), 1490–1499.
9 X. Wang, J. F. de Araújo, W. Ju, A. Bagger, H. Schmies, S. Kühl, J. Rossmeisl and P. Strasser, *Nat. Nanotechnol.*, 2019, **14**, 1063–1070.
10 A. Ozden, Y. Wang, F. Li, M. Luo, J. Sisler, A. Thevenon, A. Rosas-Hernández, T. Burdyny, Y. Lum, H. Yadegari, T. Agapie, J. C. Peters, E. H. Sargent and D. Sinton, *Joule*, 2021, **5**(3), 706–719.
11 Y. Zhu, X. Cui, H. Liu, Z. Guo, Y. Dang, Z. Fan, Z. Zhang and W. Hu, Tandem catalysis in electrochemical CO_2 reduction reaction, *Nano Res.*, 2021, **14**, 4471–4486.
12 M. K. Birhanu, M. C. Tsai, A. W. Kahsay, C. T. Chen, T. S. Zeleke, K. B. Ibrahim, C. J. Huang, W. N. Su and B. J. Hwang, *Adv. Mater. Interfaces*, 2018, **5**(24), 1800919.
13 Y. Lum and J. W. Ager, *Energy Environ. Sci.*, 2018, **11**(10), 2935–2944.
14 C. G. Morales-Guio, E. R. Cave, S. A. Nitopi, J. T. Feaster, L. Wang, K. P. Kuhl, A. Jackson, N. C. Johnson, D. N. Abram, T. Hatsukade, C. Hahn and T. F. Jaramillo, *Nat. Catal.*, 2018, **1**, 764–771.
15 C. Chen, Y. Li, S. Yu, S. Louisia, J. Jin, M. Li, M. B. Ross and P. Yang, *Joule*, 2020, **4**, 1688–1699.
16 P. Iyengar, M. J. Kolb, J. R. Pankhurst, F. Calle-Vallejo and R. Buonsanti, *ACS Catal.*, 2021, **11**(8), 4456–4463.
17 J. Huang, M. Mensi, E. Oveisi, V. Mantella and R. Buonsanti, *J. Am. Chem. Soc.*, 2019, **141**, 2490–2499.
18 D. Ren, B. Ang and B. Yeo, *ACS Catal.*, 2016, **6**, 8239–8247.
19 G. Guisbiers, S. Mejia-Rosales, S. Khanal, F. Ruiz-Zepeda, R. L. Whetten and M. José-Yacaman, *Nano Lett.*, 2014, **14**, 6718–6726.
20 S. B. Varandili, D. Stoian, J. Vavra, K. Rossi, J. R. Pankhurst, Y. Guntern, N. Lopez and R. Buonsanti, *Chem. Sci.*, 2021, **12**, 14484.
21 Y. C. Li, Z. Wang, T. Yuan, D.-H. Nam, M. Luo, J. Wicks, B. Chen, J. Li, F. Li, F. P. G. de Arquer, Y. Wang, C.-T. Dinh, O. Voznyy, D. Sinton and E. H. Sargent, *J. Am. Chem. Soc.*, 2019, **141**, 8584–8591.
22 L. Zaza, K. Rossi and R. Buonsanti, *ACS Energy Lett.*, 2022, **7**, 1284.
23 A. K. Buckley, M. Lee, T. Cheng, R. V. Kazantsev, D. M. Larson, W. A. Goddard III, F. D. Toste and F. M. Toma, *J. Am. Chem. Soc.*, 2019, **141**(18), 7355–7364.
24 J. R. Pankhurst, Y. T. Guntern, M. Mensi and R. Buonsanti, *Chem. Sci.*, 2019, **10**, 10356.
25 F. Li, Y. C. Li, Z. Wang, J. Li, D. H. Nam, Y. Lum and E. H. Sargent, *Nat. Catal.*, 2020, **3**(1), 75–82.
26 X. Kong, J. Zhao, J. Ke, C. Wang, S. Li, R. Si, B. Liu, J. Zeng and Z. Geng, *Nano Lett.*, 2022, **22**, 3801–3808.
27 L. Lin, T. Liu, J. Xiao, H. Li, P. Wei, D. Gao, B. Nan, R. Si, G. Wang and X. Bao, *Angew. Chem., Int. Ed.*, 2020, **59**(50), 22408–22413.
28 E. E. Benson, C. P. Kubiak, A. J. Sathrum and J. M. Smieja, *Chem. Soc. Rev.*, 2009, **38**(1), 89–99.

Open Access Article. Published on 18 2022. Downloaded on 14/09/25 08:51:03.
This article is licensed under a Creative Commons Attribution-NonCommercial 3.0 Unported Licence.

29 K. E. Dalle, J. Warnan, J. J. Leung, B. Reuillard, I. S. Karmel and E. Reisner, *Chem. Rev.*, 2019, **119**(4), 2752–2875.
30 E. Boutin, L. Merakeb, B. Ma, B. Boudy, M. Wang, J. Bonin, E. Anxolabéhère-Mallart and M. Robert, *Chem. Soc. Rev.*, 2020, **49**(16), 5772–5809.
31 P. Gotico, W. Leibl, Z. Halime and A. Aukauloo, *ChemElectroChem*, 2021, **8**(18), 3472–3481.
32 L. Sun, V. Reddu, A. C. Fisher and X. Wang, *Energy Environ. Sci.*, 2020, **13**(2), 374–403.
33 A. Maurin and M. Robert, *J. Am. Chem. Soc.*, 2016, **138**(8), 2492–2495.
34 M. Abdinejad, K. Tang, C. Dao, S. Saedy and T. Burdyny, *J. Mater. Chem. A*, 2022, **10**(14), 7626–7636.
35 O. S. Finikova, A. V. Cheprakov, P. J. Carroll, S. Dalosto and S. A. Vinogradov, *Inorg. Chem.*, 2002, **41**, 6944–6946.
36 K. Chen, M. Cao, G. Ni, S. Chen, H. Liao, L. Zhu, H. Li, J. Fu, J. Hu, E. Cortés and M. Liu, *Appl. Catal., B*, 2022, **306**, 121093.
37 S. Yang, Y. Yu, M. Dou, Z. Zhang and F. Wang, *J. Am. Chem. Soc.*, 2020, **142**, 17524–17530.
38 D. Gao, I. Zegkinoglou, N. J. Divins, F. Scholten, I. Sinev, P. Grosse and B. Roldan Cuenya, *ACS Nano*, 2017, **11**(5), 4825–4831.
39 Y. Wang, H. Shen, K. J. T. Livi, D. Raciti, H. Zong, J. Gregg, M. Onadeko, Y. Wan, A. Watson and C. Wang, *Nano Lett.*, 2019, **19**(12), 8461–8468.
40 G. L. De Gregorio, T. Burdyny, A. Loiudice, P. Iyengar, W. A. Smith and R. Buonsanti, *ACS Catal.*, 2020, **10**, 4854–4862.
41 A. Loiudice, P. Lobaccaro, E. A. Kamali, T. Thao, B. H. Huang, J. W. Ager and R. Buonsanti, *Angew. Chem., Int. Ed.*, 2016, **55**, 5789–5792.
42 A. Fukatsu, M. Kondo, Y. Okabe and S. J. Masaoka, *J. Photochem. Photobiol., A*, 2015, **313**, 143–148.
43 J. S. Lindsey, I. C. Schreiman, H. C. Hsu, P. C. Kearney and A. M. Marguerettaz, *J. Org. Chem.*, 1987, **52**(5), 827–836.
44 P. A. Davethu and S. P. De Visser, *J. Phys. Chem. A*, 2019, **123**(30), 6527–6535.
45 C. Römelt, S. Ye, E. Bill, T. Weyhermüller, M. Van Gastel and F. Neese, *Inorg. Chem.*, 2018, **57**(4), 2141–2148.
46 P. Gotico, W. Leibl, Z. Halime and Aukauloo, *ChemElectroChem*, 2021, **8**(18), 3472–3481.
47 R. Zhang and J. J. Warren, *ChemSusChem*, 2021, **14**(1), 293–302.
48 D. Dedić, A. Dorniak, U. Rinner and W. Schöfberger, *Front. Chem.*, 2021, **9**, 1–18.

© 2022 The Author(s). Published by the Royal Society of Chemistry